ACS EARTH AND SPACE CHEMISTRY

http://pubs.acs.org/journal/aesccq

Article

Probing Matrix Effects on the Heterogeneous Photochemistry of Neonicotinoid Pesticides, Dinotefuran and Nitenpyram

Andrea Rohrbacher, Michael J. Ezell, Véronique Perraud, and Barbara J. Finlayson-Pitts*

Cite This: *ACS Earth Space Chem.* 2021, 5, 1196–1209

Read Online

ACCESS | Metrics & More | Article Recommendations | Supporting Information

ABSTRACT: The environmental fate of neonicotinoids (NNs) is a key regulatory issue due to their widespread distribution, mobility, and role in honeybee colony collapse disorder. Here, we explore the potential matrix effects of the commercial formulations on the photochemistry of two NNs, dinotefuran (DNF) and nitenpyram (NPM). The commercial formulations and the pure reagents, both embedded in KBr pellets, were irradiated at wavelengths from 254 to 350 nm. Loss of the NN and product formation were followed using Fourier transform infrared spectroscopy and direct analysis in real time mass spectrometry. Quantum yields for loss of NN in commercial formulations were within experimental error of the pure NN. However, quantum yields for loss in KBr were consistently smaller than those previously measured for thin films of pure compounds, suggesting increased quenching of excited intermediates in the dense solid KBr matrix. At 350 nm where NPM absorbs, the quantum yield for loss in the formulation was about half that of the pure compound, which was attributed to a reduction in the NPM absorption cross section due to the presence of water taken up by additional formulation ingredients. Major products of DNF and NPM photolysis were the same in the formulation and in the pure compound. However, in contrast to previous thin film measurements, unexpected infrared peaks at 2222 and 2136 cm^{-1} during photolysis of DNF in KBr were identified as N_2O trapped in the KBr matrix and NO^+, respectively. Overall, the presence of other compounds in the formulations did not significantly alter the photochemistry compared to the pure compounds.

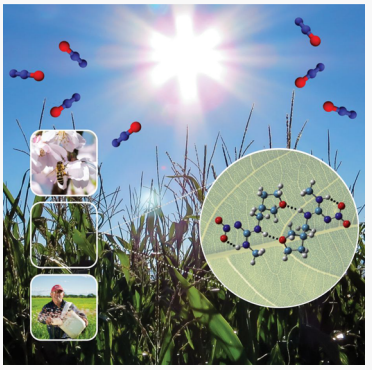

KEYWORDS: *ATR−FTIR, KBr pellet, nitrous oxide, nitroguanidine, quantum yield, emerging contaminants, insecticides*

1. INTRODUCTION

Neonicotinoids (NNs) have grown to become the most widely used insecticides globally since their introduction in the early 1990s.[1−6] The NNs are structurally differentiated into three families: nitroguanidines, nitromethylenes, and cyanamidines (Figure 1a). In addition to crop protection, they are also used in household sectors such as lawn care, in-home pest abatement, and veterinary care. NNs are neurotoxins that act by binding to specific subsites of the nicotinic acetycholine receptor.[7,8] Although these receptors are present in both insects and mammals, in vivo toxicity studies have shown that NNs are much more toxic to insects, likely due to their higher binding affinity to insect receptors.[9,10] As a result, NNs exhibit relatively low toxicity to humans, making them an attractive alternative to earlier products that have a higher potential to adversely affect human health.[11]

NNs are systemic pesticides, meaning they translocate throughout the plant tissue. This results in lower application frequency[12] and enables application as seed coatings, where the NN becomes incorporated throughout the plant tissue during growth, further reducing human exposure from the application process.[5,13] However, due to their systemic nature and prophylactic use, NNs have accumulated in the environment over time. Studies have shown that the plant may leave behind more than 95% of the NN treatment in the soil,[11,14,15] and NN residues persist in soils for years even after discontinuing their use.[16] Like other emerging contaminants, NNs can migrate through the environment and undergo chemical reactions in air, water, or soil. Their multimedia dispersal and complex multifunctional moieties make their environmental fates difficult to predict.[17−20] Indeed, NNs are commonly observed off-target on soil and vegetative surfaces,[21−25] in pollen, honey, and nectar,[26,27] on blowing dust particles during planting,[28,29] and on neighboring wildflowers and untreated plants.[22,30] Thus, although they are often initially applied as a seed coating, they are mobile and have ample opportunity for heterogeneous atmospheric chemistry on environmental surfaces that may affect their lifetimes and degradation products.

Despite their many advantages, the effect of NNs on nontarget organisms has given cause for concern.[11,31−33] Numerous studies have identified a negative impact on

Received: March 3, 2021
Revised: April 8, 2021
Accepted: April 12, 2021
Published: April 30, 2021

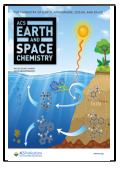

https://doi.org/10.1021/acsearthspacechem.1c00059
ACS Earth Space Chem. 2021, 5, 1196–1209

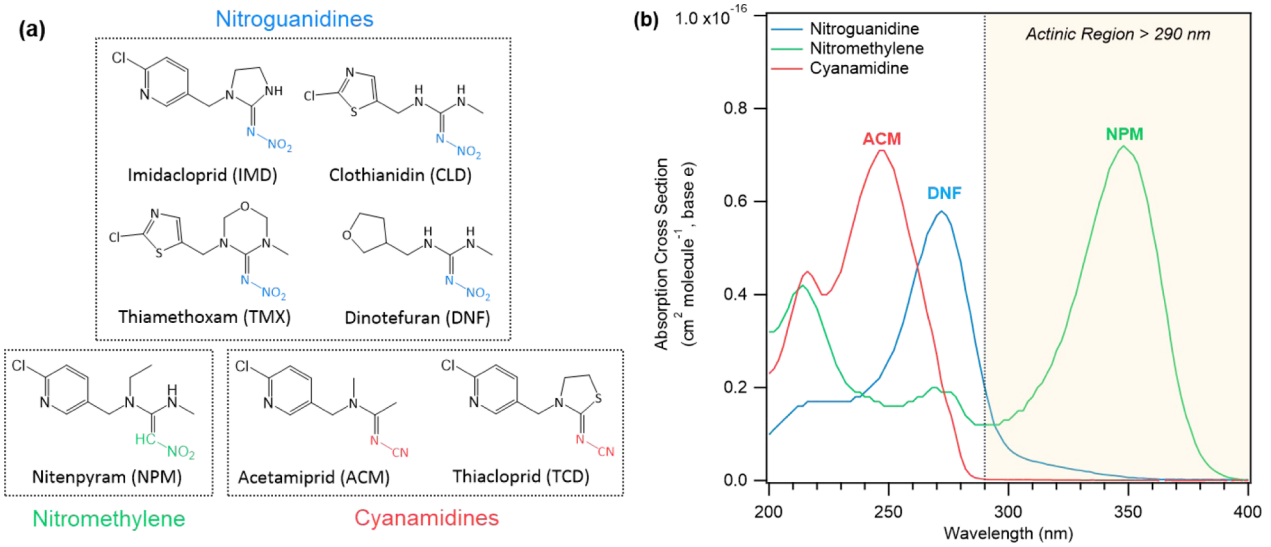

Figure 1. (a) NN subgroup structures and (b) their representative absorption cross sections given for DNF, NPM, and ACM.

pollinator health, including disease tolerance and susceptibility, navigation ability, and honeybee colony collapse disorder.[15,21,28,29,34−41] In the Woodcock et al. study,[42] NN effects on multiple bee species were evaluated at a number of different sites in the UK, Germany, and Hungary. The results were compound-, country- and species-specific but, interestingly, not always negative.[42] These location-specific effects suggest that the environmental reactions of the NNs may be playing a significant role that leads to varying impacts in different locations. This is of concern not only because NNs have shown deleterious effects on honeybees and other nontarget insects that play vital roles in our ecosystems but also because their degradation products, such as a desnitro derivative, can have increased toxicity to mammals.[43]

Based on concern for pollinator health, the EU recently introduced a moratorium on three NNs of the nitroguanidine family [imidacloprid (IMD), clothianidin (CLD), and thiamethoxam (TMX), see Figure 1a].[44,45] This work presents the heterogeneous photochemistry of two NNs that are not covered in the EU moratorium and absorb in the actinic region (Figure 1b): dinotefuran (DNF) and nitenpyram (NPM). There are hundreds of different commercial formulations available for these NN applications. These are complex mixtures consisting of many ingredients such as buffers, antioxidants, emulsifiers, and surfactants that can potentially affect degradation of the NNs. In addition, there are many different ways in which they are used, including application to the ground, injection into irrigation systems, or spraying of foliage where it can dry into a solid residue. As a result, the NNs may take many different forms in the environment which may vary from solutions to crystalline to amorphous films or deposits on solid surfaces such as dust. Earlier experiments probed thin films of the pure compounds via attenuated total reflectance (ATR)−Fourier transform infrared (FTIR) experiments, which are likely similar to NN residues on plant surfaces. This technique could not be applied to the commercial products because the additional components failed to dissolve in the solvents used to form the thin films on an ATR crystal. As a result, infrared absorbance spectra of thin films made from the dissolved commercial mixtures looked identical to those of the pure substance, indicating that only the NN active ingredient had been extracted. Thus, in the current set of experiments, the commercial mixtures and the pure NNs were dispersed in fused solid KBr pellets and probed using FTIR.

This work probes whether the two representative NNs in commercial formulations embedded in KBr pellets behave similarly to the pure reagents in KBr pellets. Previous work in this lab reported quantum yields and gas-phase N_2O yields of pure samples of seven NNs in thin films.[46−48] The results here are also compared to the thin film data and matrix effects on product formation, quantum yields, and atmospheric lifetimes are discussed.

2. EXPERIMENTAL SECTION

2.1. Preparation and Infrared Analysis of KBr Pellets.

To form the KBr pellets, potassium bromide (Fisher, Infrared grade) was ground in a mortar and pestle until it became a fine powder. Known amounts of solid NN (either pure or in the solid commercial formulation) were mixed with ground KBr in a Wig-L-Bug amalgamator for 10 s. A sample consisting of 40 mg of the NN/KBr mixture was added to 13 mm id pellet die (Pike Technologies) with stainless steel anvils and pressed under vacuum at 6−9 metric tons for 10 min. The resulting pellet had a diameter of 13 mm, and based on the density of KBr (2.74 g cm^{-3})[49] and the measured diameter and weight, the thickness was calculated to be 0.1 mm. Several pellets were probed using scanning electron microscope (SEM)−energy-dispersive system (EDS) analysis, which showed agglomerates of the NN distributed throughout the pellet (Figure S1; note the SEM images are presented for another nitroguanidine, IMD, as it has a Cl atom that is easily detectable by SEM; other NNs are expected to show similar results). The pellet was placed in a height-adjustable holder within a custom-built glass FTIR cell with CaF_2 windows (transparent to both UV and infrared light down to ~900 cm^{-1}), as shown in Figure S2. The cell was evacuated and filled with 1 atm dry N_2 (Praxair, Ultra High Purity). Earlier studies in our lab showed no significant differences between results in pure N_2 and in dry ultra-zero air.[46] The pellets were probed at measured time intervals using FTIR spectroscopy (Mattson Galaxy 5020 FTIR, cooled MCT detector) with 64 coadded scans at 0.5 cm^{-1} resolution.

https://doi.org/10.1021/acsearthspacechem.1c00059
ACS Earth Space Chem. 2021, 5, 1196−1209

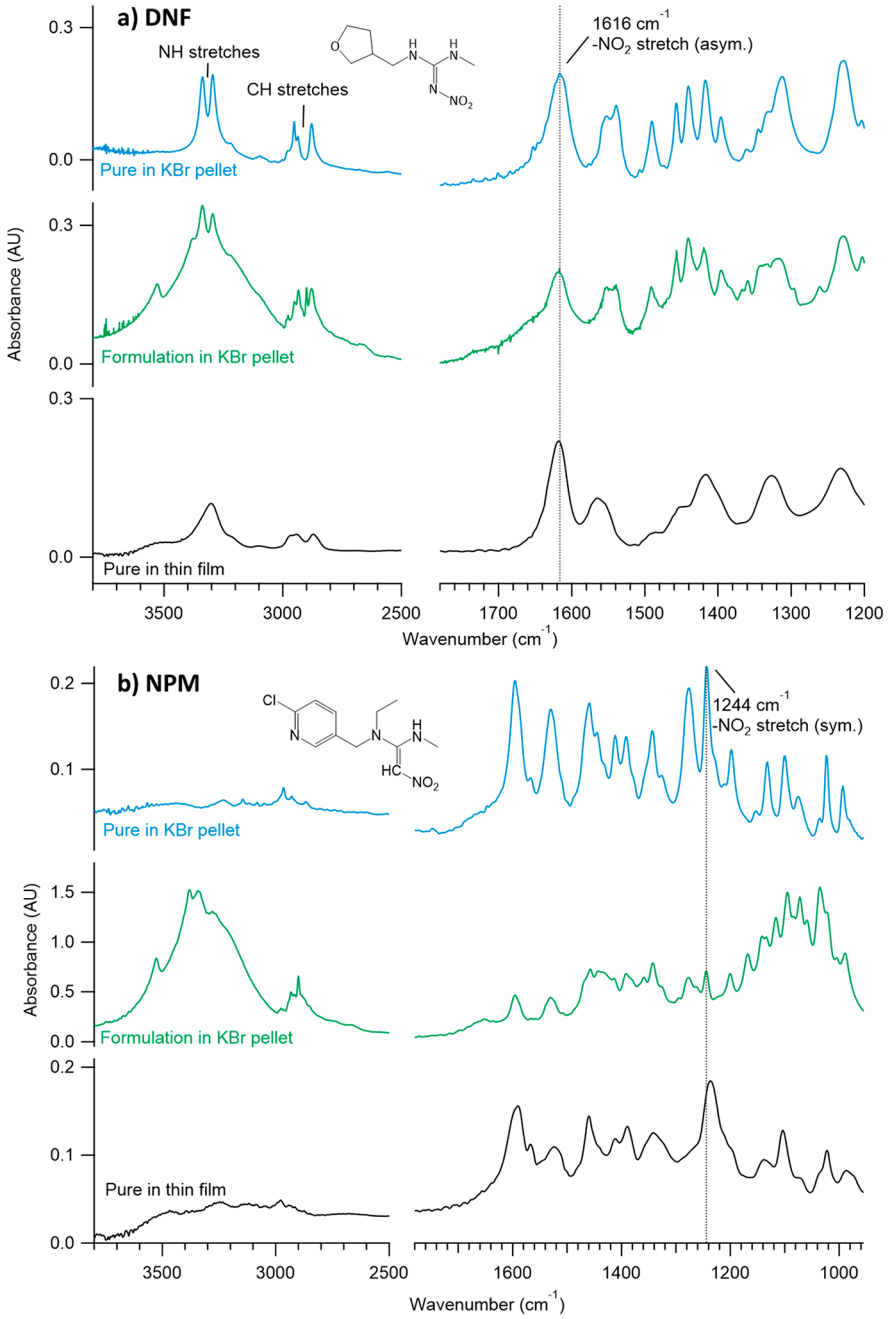

Figure 2. Absorption spectra in three forms for (a) DNF: (blue) pure DNF in a KBr pellet by transmission (3.1×10^{15} molecules/cm^2 DNF), (green) commercial formulation Safari in a KBr pellet by transmission (2.8×1015 molecules/cm^2 DNF), and (black) pure DNF in a thin film by ATR (2.4×10^{15} molecules/cm^2 DNF) and (b) NPM: (blue) pure NPM in a KBr pellet by transmission (5.9×10^{15} molecules/cm^2 NPM), (green) commercial formulation Capstar in a KBr pellet by transmission (3.8×10^{16} molecules/cm^2 NPM), and (black) pure NPM in a thinfilm by ATR (1.6×10^{16} molecules/cm^2 NPM).

Samples were irradiated using either a 254 nm low-pressure mercury lamp (UVP, CPQ-5851) or one of two mercury lamps with organic phosphor coatings that gave broadband emissions. One broadband lamp was centered at 305 nm with emission from 280 to 365 nm (Jelight, 84-2061-2), and the other was centered at 350 nm with emission from 310 to 420 nm (UVP, D-28865). Lamp emission spectra are shown in Figure S3. The 305 and 350 nm lamps provide tropospherically relevant radiation, while the 254 nm lamp was used for time-sensitive experiments as they could be completed within hours, rather than days. For example, reaching 20% photolytic degradation of the parent NN requires several hours with the 254 nm lamp but 1 week with the 305 nm lamp. A water filter was placed between the sample and the lamp to absorb heat from the lamps, and a borosilicate glass coverslip was used with the broadband lamps to filter out wavelengths below 290 nm.

Spectra were recorded with the sample in one of two positions: (1) with the rod down, so both the gas and solid KBr pellet were probed simultaneously or (2) with the rod moved up, so the pellet was out of the infrared beam and only the gas phase was measured (see Figure S2c for schematic). Subtraction of the gas phase spectrum from the combined gas and solid spectrum was used to obtain the solid-only spectrum. A single beam spectrum of a KBr pellet containing no NN was

https://doi.org/10.1021/acsearthspacechem.1c00059
ACS Earth Space Chem. 2021, 5, 1196−1209

used as the background. Spectra during photolysis were ratioed to the original pre-photolysis single beam spectrum to generate difference spectra, where positive peaks are due to product formation, while negative peaks are due to loss of the reactant.

2.2. Direct Analysis in Real Time Mass Spectrometry. Blank KBr pellets and NN/KBr pellets were further analyzed before and after photolysis using mass spectrometry (MS). The pellets were attached to a spatula and analyzed using a triple quadrupole mass spectrometer (Xevo TQS, Waters) equipped with a commercial direct analysis in real time (DART) ion source (IonSense, DART SVP with Vapur Interface). DART-MS analysis allows direct sampling of KBr pellet surfaces without the need to dissolve the solid matrix and extract the organics. The DART-MS ion source was positioned directly in front of the mass spectrometer source inlet with a 4 cm space for the sample. Helium was used as the reagent gas flowing at 3.1 L min^{-1} and subject to a grid electrode voltage of 350 V at a gas temperature of 200 °C (for NPM) or 350 °C (for DNF). Mass spectra were collected from 2 to 1000 amu using MassLynx software in the positive ion mode, where $[M + H]^+$ are the expected parent peaks.

2.3. High-Resolution Mass Spectrometry. For accurate mass measurements, solutions of NN standards were analyzed using ultrahigh-pressure liquid chromatography coupled to a diode array detector and high-resolution mass spectrometry (UPLC-DAD-HRMS) platform (ThermoScientific) equipped with a Vanquish Horizon UPLC system (including a binary LC pump, an autosampler, a column manager, and a diode array detector) coupled to a high-resolution Q Exactive Plus orbitrap mass spectrometer. Instrument and analysis details are available in Supporting Information Section D.

2.4. Preparation and Analysis of Thin Films. Thin films were also prepared for comparison to the KBr pellets. Solutions of pure NN were prepared in acetonitrile (ACN, Fisher, HPLC grade) and interrogated by ATR−FTIR. For these, ATR Ge crystals (Pike technologies, 45°, 80 mm × 10 mm × 4 mm, 10 internal reflections) were prepared by rinsing with water and ACN, followed by argon plasma cleaning for 10 min. ATR samples were prepared by pipetting 10 μL of NN solutions onto the crystals, where the solvent evaporated immediately leaving behind a thin film. These ATR samples were photolyzed and analyzed by ATR−FTIR as described in earlier studies.[46−48] For analysis using DART-MS, solutions were applied to a mesh screen (stainless steel, 74 Mesh 0.094 mm diameter), and the solvent was evaporated immediately. The NN on the mesh screen was exposed to the UV lamps and subsequently introduced into the DART source for product analysis.

2.5. Calculation of the Absolute Number of Molecules. A calibration curve was generated by depositing known volumes of NN calibration solutions in ACN (which gives the absolute number of molecules) onto the ATR crystal and recording the NN ATR−FTIR spectra absorbance immediately after the deposit dried into a thin film. ATR−FTIR absorbances were converted from mM to molecules cm^{-2} using the coated surface area of the ATR crystal (~4 cm^2). A calibration curve was generated based on the absorbance and known number of molecules cm^{-2}.

2.6. Chemicals. NNs were used in either their pure or commercial formulations. Pure NNs used were DNF (Chem Service, 98.4%) and NPM (Sigma-Aldrich, PESTANAL analytical standard). Commercial formulations were Safari and Capstar. Safari 20SG is 20% DNF w/w (Valent U.S.A. LLC, EPA Reg. no. 86203-11-59639) and also contains 1−5% sodium dodecylbenzene sulfonate buffer and 72% patent-protected inactive ingredients.[50] Capstar (10% NPM w/w, NADA #141-175), marketed as a pressed tablet, is a veterinary treatment for flea control, which is 10% NPM and includes lactose monohydrate, cellulose, starch, colloidal silicon dioxide, and magnesium stearate as inactive ingredients.[51]

3. RESULTS AND DISCUSSION

3.1. Infrared Spectra Analysis of the Pure NNs Versus Commercial Formulation. DNF and NPM samples were analyzed either in fused solids (KBr pellets) or as thin films (on an ATR crystal). In KBr pellets, the NNs were analyzed in their pure form and in commercial formulations. Infrared spectra were compared in the different forms (Figure 2), and no major differences in their infrared absorption spectra were observed. The NN fingerprints were readily apparent even in the complex commercial formulation, which is only 20% DNF or 10% NPM. For DNF in KBr, two peaks due to N−H stretches are seen in the 3000−3500 cm^{-1} region, while one broad peak is seen in the thin film spectrum. This may be due to the molecules being disordered/noncrystalline in the film while crystalline in the KBr matrix. Le Questel et al.[52] reported that DNF has a dimer crystal structure with a pair of hydrogen bonds between the N−H group of one molecule and the ring-oxygen in the neighboring DNF, as well as intramolecular hydrogen bonds between an N−H group and one of the oxygen atoms of the NO_2 group (discussed in detail below in Section 3.4, Figure 9). Thus, two distinct N−H stretches in the KBr matrix spectrum reflect two different ways of H-bonding for each of the two N−H groups in the crystal structure. In the thin film, these N−H stretches overlap, suggesting a disordered film with a variety of H-bonding rather than having two distinct H-bonding possibilities for the crystal form of the dimers. The thin films were created by evaporation from a solvent over a period of seconds, and the quick drying time may impede crystal formation.

3.2. Major NPM Photolysis Products. Figure 3 shows typical DART-MS spectra before and after irradiation for pure NPM in a KBr pellet, the commercial formulation Capstar in a KBr pellet, and a thin film of pure NPM on a mesh screen. Black traces are taken before photolysis, and colored traces are taken after 3 h of irradiation using a 350 nm broadband lamp. Similar results were observed using the 254 and 305 nm lamps. Spectra from samples before photolysis are consistent with those reported by Aregahegn et al.,[48] showing a parent peak at m/z 271 corresponding to $[NPM + H]^+$ as well as two peaks at m/z 212 and 240 corresponding to the protonated forms of the compounds below:

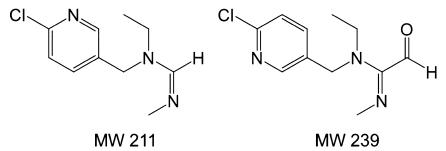

After photolysis, less contribution from m/z 271 is observed, and the peak at m/z 212 becomes dominant. The species responsible for this peak has also been previously reported in drinking water[53] and thin films.[48] The peak observed at m/z 240 was also present in all solid forms both before and after irradiation. The relative contribution from m/z 240 was higher

https://doi.org/10.1021/acsearthspacechem.1c00059
ACS Earth Space Chem. 2021, 5, 1196−1209

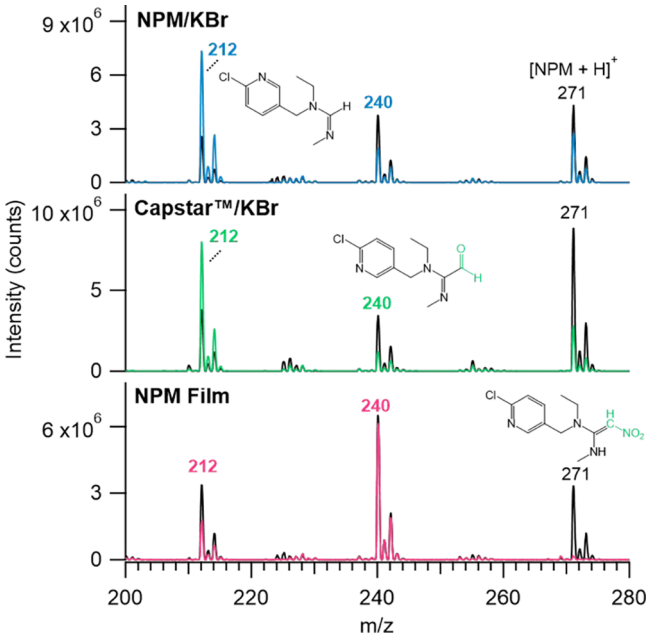

Figure 3. DART-MS of NPM before (black traces) and after (color traces) photolysis at 350 nm for 3 h in three solid forms.

in thin film samples both before and after photolysis and may be due to its formation in the DART source itself.[48]

Evidence for both of these products is also found in the infrared difference spectra of photolyzed NPM (Figure 4), where positive peaks indicate formation of products and negative peaks indicate loss of NPM. In all three solid forms, a major positive product peak is observed at 1636 cm^{-1}, a region characteristic of C═N bonds.[54] In thin films, a second product

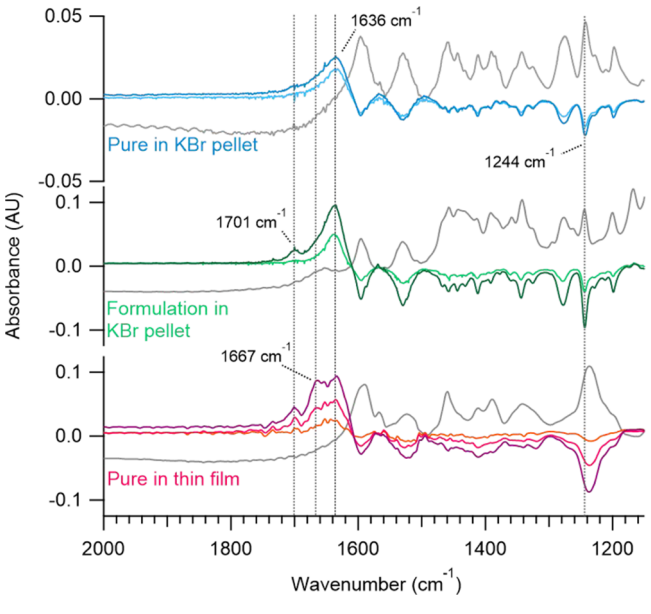

Figure 4. NPM irradiated at 305 nm in three matrices: (blues) pure NPM in a KBr pellet (5.9×10^{15} molecules/cm^2 NPM at 35 and 50% loss), (greens) commercial formulation Capstar in a KBr pellet (3.8×10^{16} molecules/cm^2 NPM, 20 and 48% loss), and (pinks) pure NPM in a thin film (2.7×10^{16} molecules/cm^2 NPM at 16, 50 and 92% loss). Gray traces show initial absorbance spectra before photolysis. The initial absorbance spectrum of the commercial formulation has been multiplied by a factor of 0.1.

peak is also distinguishable at 1667 cm^{-1}, and although not prominent in the pure and formulated NPM embedded in KBr, it is likely contributing to the broad 1636 cm^{-1} peak shape. Aregahegn et al.[48] attributed the 1667 cm^{-1} peak to the C═N stretch of the MW 211 species and a 1634 cm^{-1} peak to the C═N stretch of the MW 239 species, red-shifted due to conjugation with the C═O group. A small peak for the C═O stretch is also visible at 1701 cm^{-1}.

The apparent smaller contribution of the MW 211 species at 1667 cm^{-1} in the infrared difference spectra compared to the DART-MS may be due to differences in absorptivity. Although reference standards of NPM degradation products were not available, those for products from the NN IMD which contain C═O and C═N bonds show that the C═O containing species has higher infrared absorptivity at equimolar concentrations (Figure S4). Similarly, DART-MS spectra are influenced by variable ionization efficiency across compounds, gas reagent temperature, vapor pressure of the species, and heterogeneity of the pellet. Thus, neither DART-MS nor FTIR relative intensities should be assumed to reflect their relative contributions. The combination of MS and FTIR data, however, suggest that both species are present as photolysis products in pure and commercial formulations.

3.3. Major DNF Photolysis Products: Desnitro and Urea Pathways. Figure 5 shows typical DART-MS spectra for

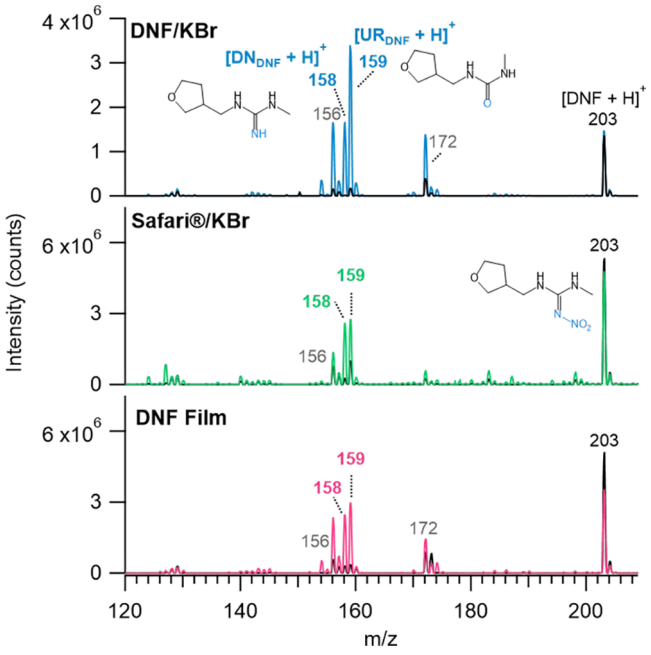

Figure 5. DART-MS of DNF before (black traces) and after (color traces) photolysis at 305 nm in three solid forms.

DNF in the three forms before photolysis and after 15 h of irradiation using a 305 nm broadband lamp. Before photolysis (black traces), DNF (MW 202) shows a parent peak at *m/z* 203 corresponding to $[DNF + H]^+$ as well as a dimer ion at *m/z* 405 corresponding to $[2DNF + H]^+$ (data not shown). MS/MS analysis of *m/z* 203 (Figure S5) showed fragments at *m/z* 157, 129, and 113, consistent with the literature for DNF.[55−59]

After photolysis (Figure 5, colored traces), product peaks corresponding to urea (UR_{DNF}) and desnitro (DN_{DNF}) derivatives appear, which are commonly observed for samples

https://doi.org/10.1021/acsearthspacechem.1c00059
ACS Earth Space Chem. 2021, 5, 1196−1209

Scheme 1. Proposed DNF Degradation Mechanism, Following Wang et al. 2019[46] and Aregahegn et al. 2016[47]

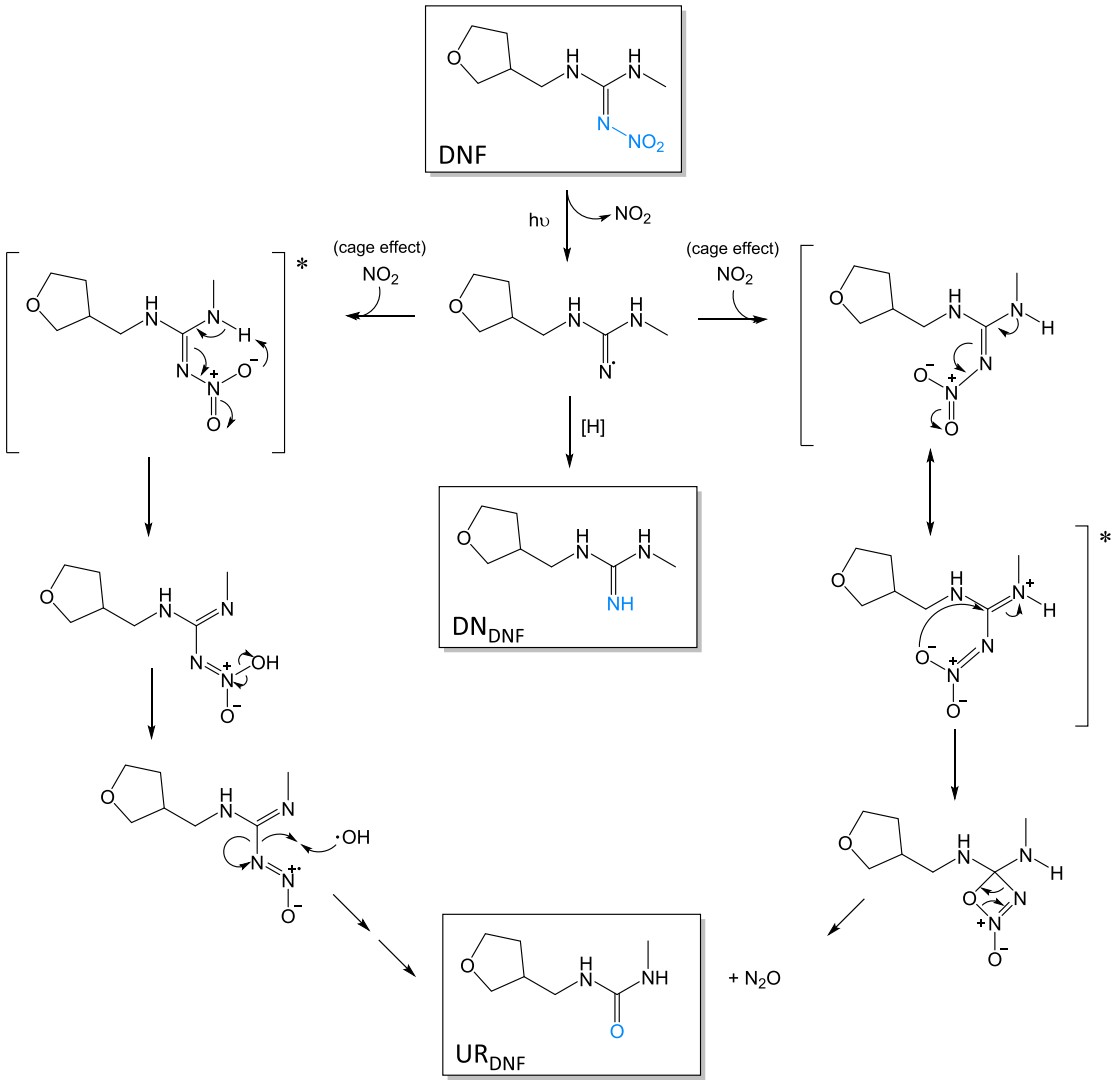

containing DNF and its metabolites.[55,57,58,60] UR_{DNF} (MW 158) is seen at *m/z* 159 corresponding to $[UR_{DNF} + H]^+$ as well as at *m/z* 317 and *m/z* 361 (data not shown) corresponding to $[2UR_{DNF} + H]^+$ and $[UR_{DNF} + DNF + H]^+$, respectively. The peak at *m/z* 158 corresponds to $[DN_{DNF} + H]^+$ for the desnitro derivative DN_{DNF} (MW 157). MS/MS spectra are shown in Figure S6, and a fragmentation mechanism consistent with the major fragments is provided in Scheme S1. Peaks were also observed at *m/z* 156 and *m/z* 172 before and after photolysis. These peaks were further explored using UPLC-DAD-HRMS (Table S1), which identified them as $[C_7H_{14}ON_3]^+$ attributed to $[DNF - NO_2]^+$ and $[C_7H_{14}O_2N_3]^+$ attributed to $[DNF - NO]^+$. The species' retention time and peak shape were identical to that of the parent *m/z* 203 species and are thus believed to be due to in-source fragmentation, in agreement with their presence in the pre-photolysis DART-MS spectra. Therefore, for DNF in all matrices, DN_{DNF} and UR_{DNF} are the major solid photolysis products, and their proposed formation mechanism is shown in Scheme 1.

The infrared difference spectra of photolyzed DNF (Figure 6) show a product peak near 1665 cm^{-1}. The broad peak shape again likely indicates overlapping contribution from the C═O and C═N stretch signals of the urea and desnitro products, as was the case for photolysis of thin films of structurally similar IMD,[47] and shown in KBr pellets in Figure S4.

The formation of the urea and desnitro derivatives is of great importance for two reasons. First, both are still expected to exhibit insect toxicity. Second, while the urea derivative has low toxicity to mammals, the desnitro derivative may show a large increase in mammalian toxicity. For example, Chao and Casida[43] reported that for IMD degradation products, DN_{IMD} has an oral LD_{50} of 7−24 mg/kg in rats, an increase from the 424 mg/kg of the parent IMD, and is more toxic than nicotine, which has an oral LD_{50} of 50 mg/kg. These photolysis products are expected to remain on surfaces, where they can be a risk for both pollinators due to their insect toxicity as well as to consumers of treated foods due to the increased mammalian toxicity of the desnitro derivative. There are no direct mammalian toxicity measurements of UR_{DNF} and DN_{DNF} which would be important for a full evaluation of their environmental impacts.

3.4. Unexpected "Solid Phase" Products. DNF difference spectra (Figure 6) also show new solid-phase product peaks at 2222 and 2136 cm^{-1}, a region characteristic of ν(NO) stretches.[61] These products were observed in both pure and

https://doi.org/10.1021/acsearthspacechem.1c00059
ACS Earth Space Chem. 2021, 5, 1196−1209

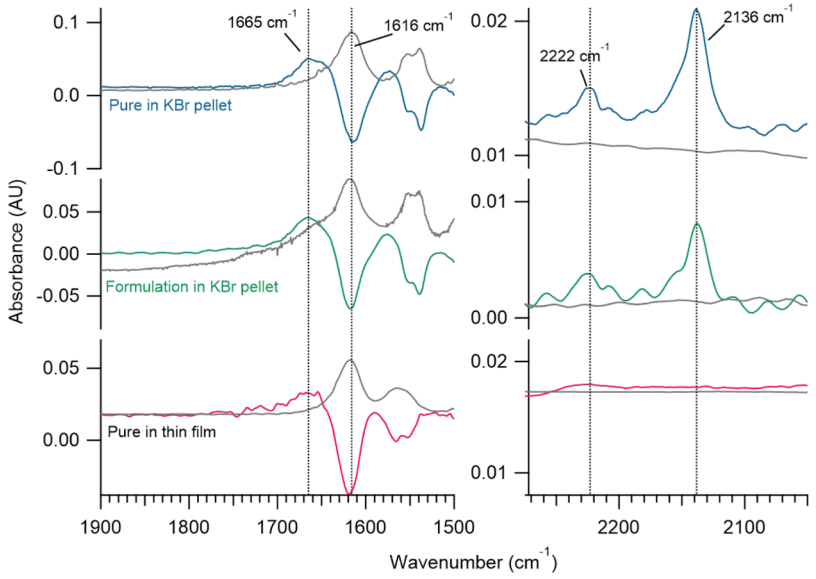

Figure 6. Solid-phase difference spectra of DNF irradiated at 305 nm in three matrices: (blue) pure DNF in a KBr pellet by transmission (3.1×10^{15} molecules/cm^2 DNF, 43 % loss), (green) commercial formulation Safari in a KBr pellet by transmission (2.8×10^{15} molecules/cm^2 DNF, 31% loss), and (pink) pure DNF in a thin film by ATR (2.4×10^{15} molecules/cm^2 DNF, 36% loss). Gray traces show initial absorbance spectra before photolysis for reference only, not to scale.

formulated DNF samples in the KBr matrix, indicating again that the presence of the additional ingredients in the formulations did not affect the product distribution. These peaks, however, were not strongly seen in irradiated thin films of DNF, suggesting that the dense solid KBr pellets do affect the photodegradation.

The 2222 cm^{-1} solid-phase peak overlapped with product peaks observed in the gas phase. Figure 7 shows a broad peak

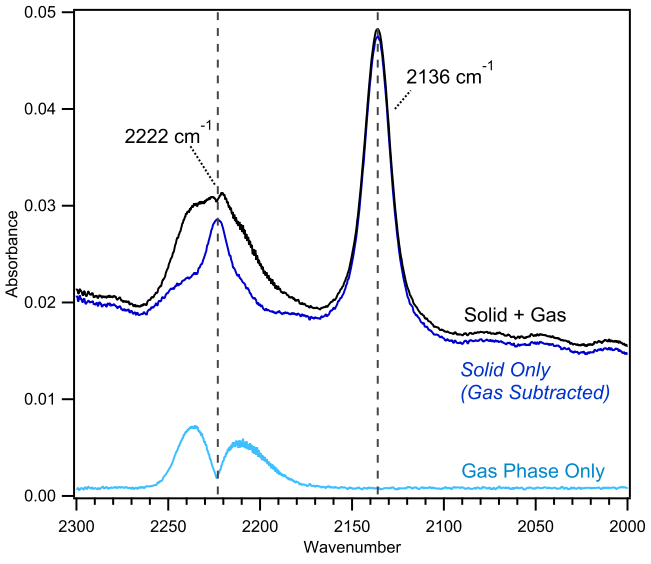

Figure 7. FTIR spectra comparing solid- and gas-phase products of 0.5% DNF/KBr photolyzed at 254 nm to 59% loss DNF.

around 2222 cm^{-1} that is observed with the sample rod in the down position, probing both the solid and gas phases simultaneously. When the rod was raised to probe the gas phase only, N_2O, with its distinct *P* and *R* branches,[62] was clearly evident. In earlier studies, N_2O was hypothesized to be formed from cleavage of the N–NO_2 bond in nitroguanidines (such as DNF) and the C–NO_2 bond in NPM, followed by intramolecular rearrangements in the solids.[46−48] Subtraction of the gas phase from the combined gas and solid spectra reveals a broad peak in the solid centered at 2222 cm^{-1}. This product in the solid phase was observed also for a number of NNs (Figure 8), all of which form N_2O in the gas phase when irradiated as thin films.[46] Dows[63] and Yamada and Person[64] showed that condensed N_2O at 80 K has a single peak in this region, with some variation in peak shape, and Hisatsune[65] showed a temperature dependence for this peak's location and shape. Thus, we assign the 2222 cm^{-1} peak seen in the solid-only spectrum to N_2O that is trapped in the KBr pellet solid.

This peak was not seen when irradiating DNF in a solid pellet made of Cabosil (Cabot Corporation), which is an ultrafine silica oxide powder, but N_2O was observed in the gas phase, suggesting that N_2O was not efficiently trapped in the Cabosil environment. The reason for the difference between Cabosil and KBr matrix is not clear, but it may be due to the strongly ionic environment in KBr or due to differences in the particle size and packing that can influence the trapping.

DNF in a KBr pellet also showed a product peak at 2136 cm^{-1} (Figures 6 and 8). Bands in this region have often been identified as being due to the nitrosonium ion (NO^+)[66−74] in studies of the interaction of NO_x with zeolites (although adsorbed NO_2 has also been suggested).[75] This peak was also not seen in the Cabosil matrix, suggesting that NO^+ is stabilized by the ionic KBr environment.

If the NO_2 generated upon bond cleavage is free to migrate in the matrix, it could react with the KBr to form NO^+. To test this, a KBr pellet (with no NN present) was exposed to 293 ppm NO_2 in both static and flow modes, with and without photolysis, but a peak at 2136 cm^{-1} was not observed. As expected, gas-phase NO_2 peaks (1617 and 2906 cm^{-1}), a BrNO peak (~1800 cm^{-1}), and a solid NO_3^- peak (1358 cm^{-1}) were observed, consistent with earlier studies of the reaction of NO_2 with NaBr.[76] None of these were observed in the DNF/KBr photolysis experiments. This suggests that when NO_2 is formed in the DNF photolysis, it undergoes

https://doi.org/10.1021/acsearthspacechem.1c00059
ACS Earth Space Chem. 2021, 5, 1196−1209

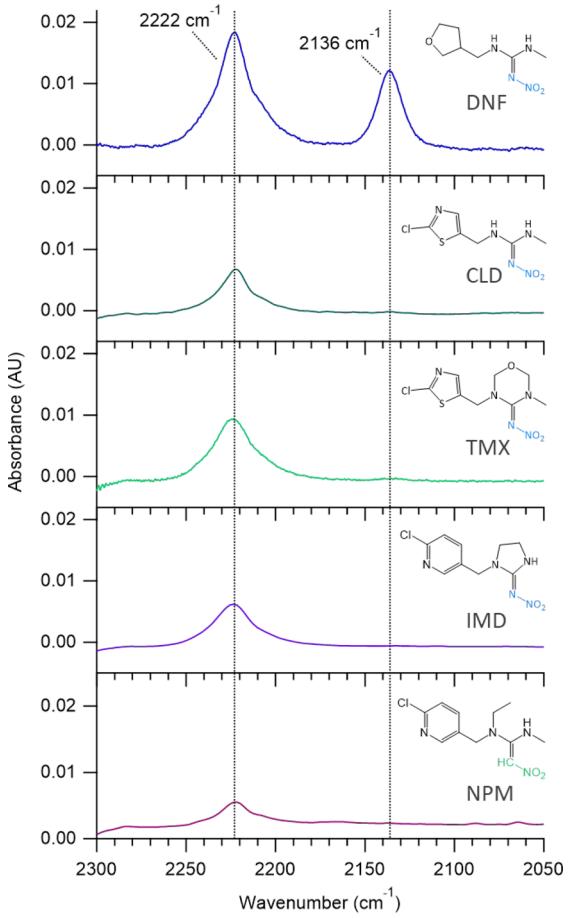

Figure 8. Comparison of solid-phase product formation in KBr pellets at w/w concentrations of 0.49% DNF/KBr, 1.04% CLD/KBr, 0.94% TMX/KBr, and 0.94% IMD/KBr, and 0.67% NPM/KBr. Nitroguanidines were irradiated at 254 nm for ~30 min and NPM for 10 h.

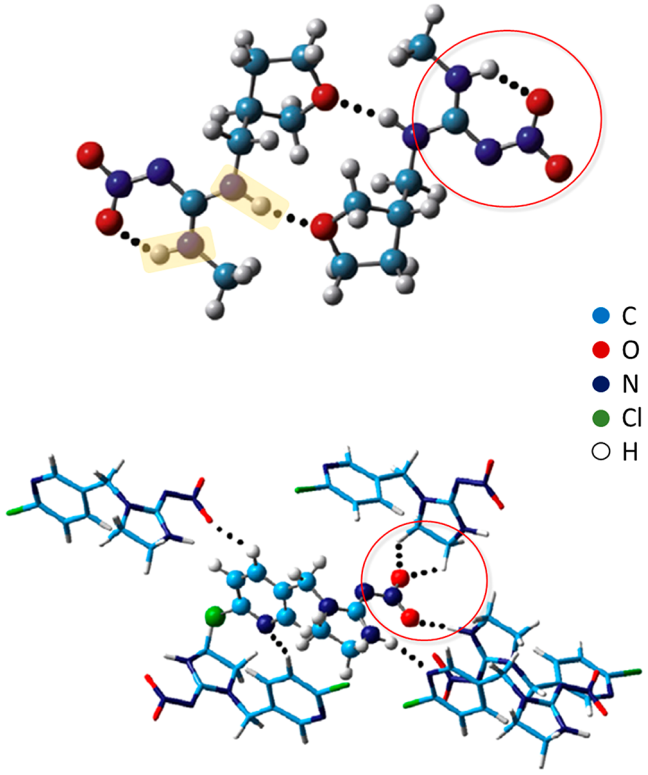

Figure 9. Crystal structures of DNF (top) and IMD (bottom). The red circles highlight the differences between DNF and IMD in -NO_2 hydrogen bonding. The yellow coloring on DNF highlights the two types of N–H stretches observed in the infrared spectra. Adapted from Le Questel, J. Y.; Graton, J.; Ceron-Carrasco, J. P.; Jacquemin, D.; Planchat, A.; Thany, S. H. New insights on the molecular features and electrophysiological properties of dinotefuran, imidacloprid and acetamiprid neonicotinoid insecticides. *Biorg. Med. Chem.* **2011**, *19* (24), 7623–7634. Copyright 2011, Elsevier.[52]

recombination and intramolecular rearrangements shown in Scheme 1 rather than reacting with KBr. This is reasonable since the DNF exists as agglomerates of the NN within the KBr matrix (Figure S1), rather than as individually distributed molecules.

The 2136 cm^{-1} peak was only seen in the solid-phase spectra and was only weakly present, if at all, in the other NNs in KBr pellets (Figure 8). In the thin films of DNF and the structurally similar nitroguanidine CLD, a small peak is seen initially but disappears within minutes, while in the KBr pellet, it is detectable for days. A possible explanation is the crystal structure of DNF (Figure 9) reported in Le Questel et al.[52] DNF crystallizes into a dimer structure, connected by hydrogen bonds between the ring and one of the secondary amines in the nitroguanidine group. Note that only one of the $-NO_2$ group oxygen atoms is intramolecularly hydrogen bonded, in contrast to IMD, for example. This may assist in isomerization to –ONO, which is a known intermediate in the photolysis of nitro-organics[77,78] and subsequent generation of NO^+ (Scheme 2). For example, Bhattacharya et al.[79] in an experimental and theoretical study of the photolysis of dimethylnitramine, $(CH_3)_2N–NO_2$, which shares structural features similar to DNF, report that a nitro/nitrite isomerization mechanism is the major channel of decomposition from the excited electronic state for photolysis in a dense gaseous medium. In the IMD crystal structure in Figure 9, on the other hand, there are three intermolecular hydrogen bonds with the $-NO_2$ group. Thus, the $-NO_2$ may be too constrained for isomerization to –ONO. The other nitroguanidines, with a similar ring structure to IMD, may be expected to behave the same way. This further suggests that samples in the fused solid KBr pellet are in their crystalline form but in a disordered form in the thin films with a variety of hydrogen bonding possibilities.

3.5. Change in Products after Photolysis. If the 2222 cm^{-1} peak is due to N_2O trapped in the solid, it might be expected over time to decrease as the N_2O diffuses to the gas phase. To test this, the DNF/KBr pellet was irradiated with the 254 nm lamp to ~20% loss of DNF, then the light was turned off, and FTIR spectra were continually recorded to monitor both products in the KBr pellet as well as the gas phase. These experiments were conducted using the 254 nm lamp to give relatively rapid photodegradation and product formation compared to the longer times over which diffusion is expected to occur. Figure 10 shows signal intensities in either solid-phase or gas-phase spectra for reactant and product peaks from before photolysis (time = 0 min), during photolysis (first 30 min), and for four days after the lamp is shut off (gray area). The corresponding changes in the FTIR spectra are shown in Figure 11. The first data point in Figure 10, taken before photolysis begins, shows a non-zero value only for the DNF signal (Figure 10a). The second data point, obtained after the sample has been irradiated for 30 min, shows a decrease in

https://doi.org/10.1021/acsearthspacechem.1c00059
ACS Earth Space Chem. 2021, 5, 1196–1209

Scheme 2. Proposed Isomerization of $-NO_2$ to $-ONO$ to Produce NO^+.

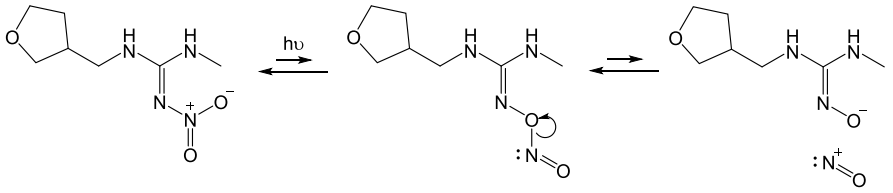

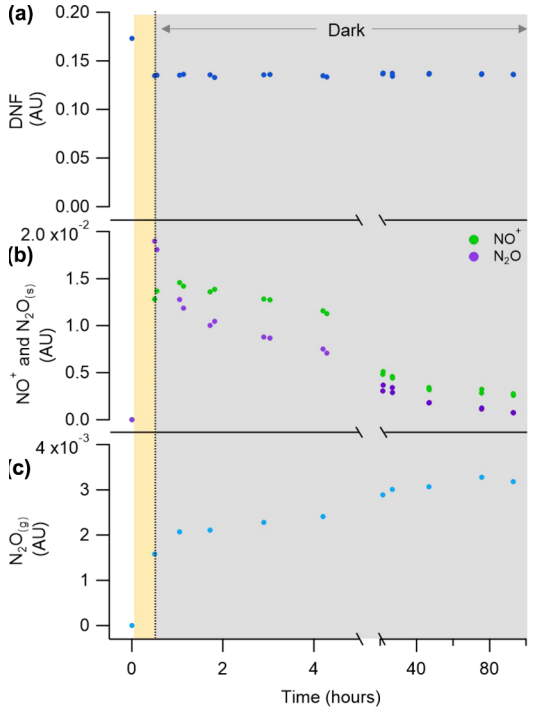

Figure 10. 0.49% DNF/KBr irradiated at 254 nm to 21% loss DNF (dashed line) and then monitored for 4 days in dark conditions. Frames (a,b) are of solid phase-only spectra (gas phase has been subtracted) and results in (c) for $N_2O(g)$ are taken from gas phase-only spectra. *Y*-Axis is the absorbance peak height for (a) DNF at 1616 cm^{-1} and (b) product peak heights for NO^+ (2136 cm^{-1}) and $N_2O(s)$ (2222 cm^{-1}) products, and (c) $N_2O(g)$ peak measured at 2235 cm^{-1} from the gas-phase spectra.

DNF and positive values for all products formed (Figure 10b,c), The DNF signal is nearly constant over the 4-day dark period. The peak at 2222 cm^{-1}, assigned to trapped N_2O, decreased to near zero by the end of the 4 days. The same was true of the 2136 cm^{-1} peak assigned to NO^+. Simultaneously, gas-phase N_2O increased, as expected, if the N_2O trapped in the solid was diffusing out into the gas phase. No other new peaks, for example, due to NO, NO_2, or BrNO, were detected in the gas phase, suggesting that recombination to reform the nitrite ($-ONO$) and DNF may be the major fate of NO^+ (Scheme 2). In this case, the relative change of DNF signal may be too small to show a significant signal change over time.

The DNF/KBr pellet from the light/dark study was also analyzed using DART-MS after the 4-day dark period. There were no new peaks observed after the dark period when compared to the sample analyzed immediately after photolysis. Similar light/dark experiments using the 305 nm lamp, which required a week of photolysis to reach 20% loss of DNF, gave qualitatively similar results but less solid N_2O infrared peaks due to the slower rate of formation relative to diffusive loss to the gas phase. When the lamp was removed to begin the dark period, the solid N_2O peak completely disappeared within 1 day, and the $N_2O(g)$ signal increased slightly during this first day corresponding to escape from the solid phase.

3.6. N_2O Yields. Gas-phase N_2O yields (Δ moles N_2O/Δ moles NN) were calculated for the KBr pellet experiments after the solid phase peak at 2222 cm^{-1} had disappeared and the gas phase N_2O signal had stabilized. KBr pellet experiments showed a yield of 0.51 ± 0.10 for both pure DNF and the commercial formulation Safari. Table 1 shows that these values are in agreement with previously reported values for pure solid deposits on windows using the transmission mode but lower than that when ATR was used on thin films.[46] This suggests

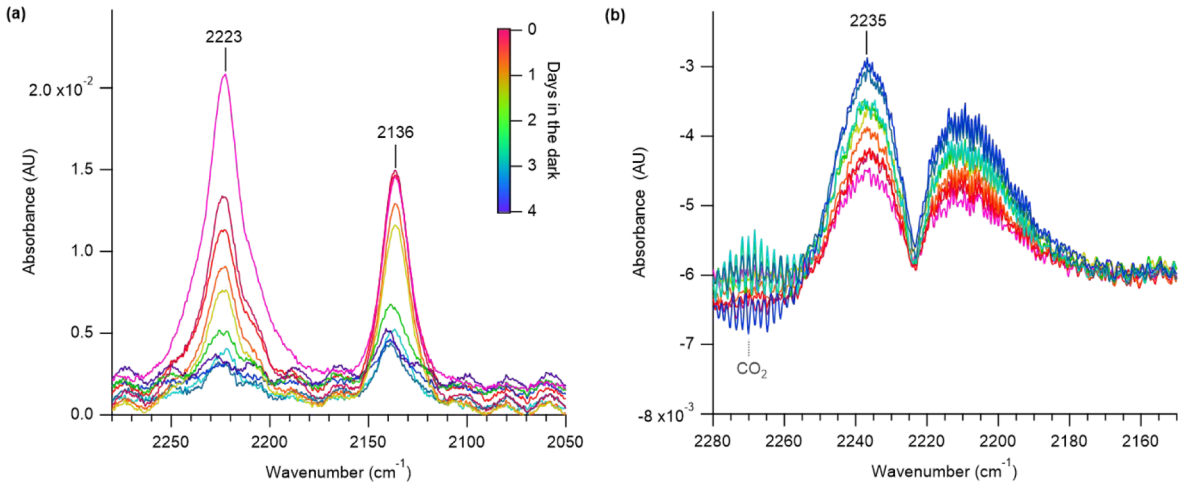

Figure 11. 0.49% DNF/KBr irradiated with a 254 nm lamp for 30 min (pink trace). The photolysis lamp was shut off, and the sample was then monitored for 4 days in dark conditions. Spectra are (a) solid phase only and (b) gas phase only.

https://doi.org/10.1021/acsearthspacechem.1c00059
ACS Earth Space Chem. 2021, 5, 1196−1209

Table 1. Nitrous Oxide Yields ($\Delta[N_2O]/\Delta[NN]$) from Photolysis of DNF in Different Matrices

matrix	method	N_2O yield[a]
pure in KBr pellet	transmission	0.51 ± 0.10
formulation in KBr pellet	transmission	0.51 ± 0.10
pure NN deposits on window[46]	transmission	0.57 ± 0.38
pure in thin film[46]	ATR	0.94 ± 0.40

[a]Errors are 2σ, calculated as $\sigma = \left(\frac{\sum(x_i-\mu)^2}{N}\right)^{1/2}$.

that the branching ratio that leads to N_2O is altered in the KBr pellets and the window deposits compared to the thin ATR films. NPM also generates N_2O, although at a much lower yield than the nitroguanidines (yield of ∼0.1 for NPM in thin films compared to ∼1.0 for nitroguanidines in thin films).[46] Evidence for some trapped N_2O was also observed in NPM that may affect these N_2O yields but was too small to be quantified.

The major source of tropospheric N_2O is known to be nitrification and denitrification in soils and aquatic systems. Nitrous oxide soil emissions are characterized by very high spatio-temporal variability resulting in "hot spots" and "hot moments,"[80] which are believed to be driven mainly by abiotic inputs such as fertilizers.[81−83] While N_2O from photolysis of the NNs will be a minor contributor to the overall global burden,[46,47] it could contribute to these hot spots.

3.7. Quantum Yield Calculations for Loss of NN during Photolysis. Loss of DNF and NPM was followed using the 1616 and 1244 cm^{-1} peaks (assigned to the asymmetric and symmetric $-NO_2$ stretches, respectively).[46,54] The decays followed first-order kinetics. An interesting pattern was observed in the photodegradation rate constants from 254 nm irradiation, as shown in Figure S7, where higher concentrations of NN in the KBr pellets resulted in lower photolysis rate constants. Since the SEM−EDS images showed the NN present as agglomerates spread throughout the pellet, this suggests that at higher concentrations, these agglomerates may be physically shielding NN molecules located deeper in the pellet. Therefore, lower concentration photolysis rate data were considered to be more accurate, and these were used for quantum yield calculations.

Photolysis quantum yields (ϕ) for loss of either DNF or NPM were calculated using eq 1[84]

$$k_p = \phi \sum \sigma(\lambda)\cdot I_{rel}(\lambda)\cdot CF \quad (1)$$

Absorption cross sections (σ) in base 10 were measured using solutions of known NN concentrations and converted to base e (Figure 1b). The absolute light intensity was measured using 2-nitrobenzaldehyde (2NB) as an actinometer with a well-established photolysis quantum yield of 0.5 in a solid.[85−88] The correction factor, *CF*, converts relative to absolute lamp intensities as described in the Supporting Information, Section I and Figure S8. Photolysis rate constants (k_p) for the NN were obtained from their first-order plots (Figure S9) and are summarized in Table S2. The quantum yields relevant to the actinic region for both DNF and NPM measured using the 305 nm and 350 nm broadband lamps are reported in Table 2 and Figure 12. Quantum yields at 254 nm and in previous work[46,48] probing thin films of pure NNs are also provided for comparison.

In KBr pellets, quantum yields are lower by a factor of ∼5−10 than in thin films across all irradiation wavelengths. This is likely due to the high-density KBr matrix. As discussed in detail in previous papers[46−48] and shown in Scheme 1, the first step in the photolysis is scission of the $-NO_2$ bond. Recombination with the organic fragment simultaneously formed releases the bond energy into the regenerated molecule, precipitating a set of internal rearrangements and reactions that lead to the observed products. The presence of the high-density solid matrix likely damps some of the excess energy, resulting in lower quantum yields observed in the KBr pellets.[17,89]

There were no significant differences in quantum yields at 254 and 305 nm between the pure and formulated DNF in a KBr matrix (Table 2). This was also true for NPM at both wavelengths. However, at 350 nm, the NPM quantum yield in the formulation decreased by about a factor of 2 compared to pure NPM in KBr pellets (Table 2). Uptake of water into the KBr pellet by the additional ingredients in the commercial formulation, which includes such compounds as silica (a well-

Table 2. Comparison of Quantum Yields

neonicotinoid	lamp (nm)	ϕ ($\times 10^{-3}$)[a] pure NN (KBr pellet)	formulation (KBr pellet)	pure NN (thin film)[46,48]
DNF	254	1.5 ± 0.6	1.8 ± 0.7	8.6 ± 2.3
	305	0.35 ± 0.14	0.37 ± 0.19	3.3 ± 0.5
NPM	254	1.1 ± 0.5	1.6 ± 0.5	12 ± 4
	305	0.21 ± 0.11	0.21 ± 0.08	1.0 ± 0.3
	350	0.20 ± 0.06	0.084 ± 0.04[b]	0.94 ± 0.15

[a]Quantum yield (ϕ) is defined as the rate of loss of NN divided by the rate of absorption of photons. Each entry should be multiplied by 10^{-3}, for example, the first quantum yield is $(1.5 \pm 0.6) \times 10^{-3}$. Standard deviation ($1\ \sigma_\phi$) is determined by uncertainties in the NN photolysis rate constants (k_{NN}) and the measurement of the intensity CF from the 2NB photolysis rate constant (k_{2NB}), calculated as: $\frac{\sigma_\phi}{\phi} = \left[\left(\frac{\sigma_{k_p}}{k_p}\right)^2 + \left(\frac{\sigma_{CF}}{CF}\right)^2\right]^{1/2}$ where uncertainties in $\Sigma\sigma I$ are taken to be negligible compared to those in k_p and CF. [b]The quantum yield at 350 nm for NPM has not been corrected for a possible change in the absorption cross section due to adsorbed water. The value shown is therefore a lower limit.

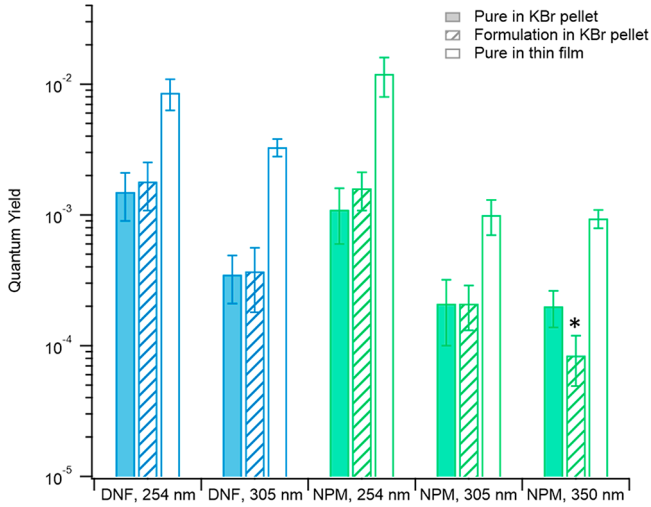

Figure 12. Quantum yields for pure NN in thin films and pure and formulated NN in KBr pellets. Errors are ± 1 σ. The asterisk (*) indicates that the quantum yield at 350 nm for NPM has not been corrected for a possible change in absorption cross section due to adsorbed water. The value shown is therefore a lower limit.

https://doi.org/10.1021/acsearthspacechem.1c00059
ACS Earth Space Chem. 2021, 5, 1196−1209

known desiccant), cellulose, and starch, could alter the effective absorption cross section at 350 nm since UV−vis absorption cross sections for NPM in the 350 nm region are greatly reduced in the presence of water.[90] As shown in Figure 13, UV−vis absorption spectra do indeed show reduced

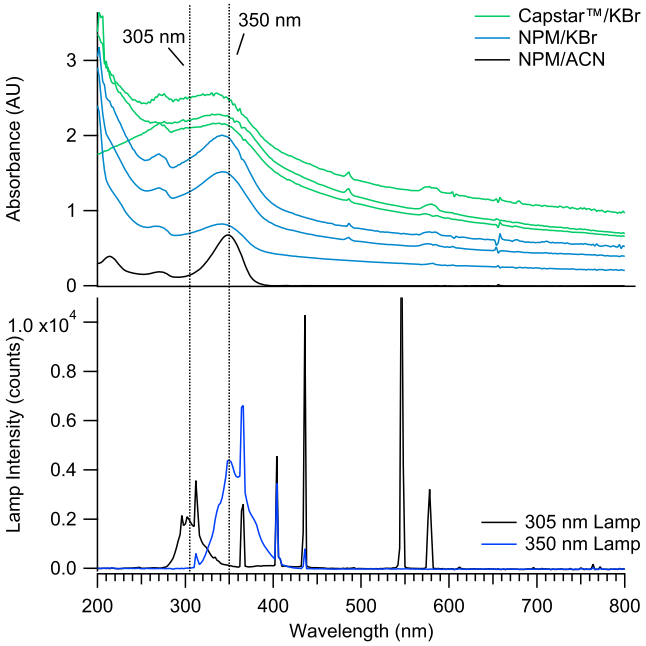

Figure 13. UV−vis absorbance spectra (top) of 0.36 mM NPM in ACN, 0.48% NPM/KBr (w/w), and 4.8% Capstar/KBr and photolysis lamp emission spectra (bottom). Obtaining quantitatively reproducible spectra of solids is difficult due to the inhomogeneity of the pellets and light scattering differences, so three runs of each were carried out. The three green and three blue spectra are replicate runs of Capstar in KBr and NPM in KBr, respectively.

relative absorption near 350 nm for the Capstar/KBr pellets compared to pure NPM in the KBr pellet or NPM in ACN solution. Comparison to the lamp emission spectra also shown in Figure 13 shows that this shift in absorbance would affect quantum yield calculations for the 350 nm lamp much more than the 305 nm lamp calculations. In that case, the true quantum yield may in fact not change significantly at 350 nm in different matrices.

It should be noted that the absorption cross sections used for the calculated quantum yields of NN in KBr pellets were for the NN in solution. Absorption cross sections in the KBr pellet were highly variable due to pellet inhomogeneity (Figure 13) but did not show significant differences qualitatively from the solution spectra. Thus, for the purpose of comparing the pure NN to the commercial formulation, we found it sufficient to use one consistent absorption cross section represented by the NN in solution.

4. CONCLUSIONS

NNs are the only new major insecticide class introduced in the last 30 years, and their presence throughout the environment puts them in contact with pollinators and humans. When considering the fate of the NNs in the environment, it is important to note that the high-pressure environment required to form KBr pellets, which is responsible for the difference in degradation rates observed here, is not representative of field conditions. Therefore, quantum yields, lifetimes, and products predicted using thin films are likely more relevant to field conditions. The KBr pellet process was essential, however, to compare the commercial formulation to the pure NN, which showed that laboratory experiments using the pure reagents can be representative of the commercial formulations.

The present studies show that the N_2O and quantum yields from photolysis of DNF and NPM are relatively insensitive to the presence of inert commercial formulation ingredients. Calculated quantum yield values for loss of NPM at 350 nm, however, were reduced by about a factor of 2 in the commercial formulation which is attributed to reduced absorption cross sections arising from uptake of water by the additional formulation ingredients. Major photodegradation products in KBr pellets were also similar in the pure NNs and commercial formulations. Major DNF photodegradation products include a desnitro and urea derivative. By analogy to IMD, the desnitro product may have increased toxicity[43] compared to the parent compound.

There were two unexpected products observed by infrared in the fused solid KBr matrix of both pure and commercial formulations that are not observed in the thin film irradiations. One which was observed in significant intensity only in the photolysis of DNF was assigned to NO^+. Structural insights into why this NN behaved differently points to the dimer crystal structure of DNF where only one of the oxygens in the $-NO_2$ group is involved in hydrogen bonding, in contrast to IMD, for example, where both $-NO_2$ oxygens are hydrogen bonded. The single hydrogen bond in DNF may facilitate isomerization to −ONO in the excited state, which led to production of NO^+ in the ionic KBr matrix.

The second unexpected product using KBr pellets was determined to be N_2O trapped in the solid phase, which was observed to diffuse to the gas phase over time. This was seen in all NNs that generate gas-phase N_2O. Trapped N_2O was observed in fused solid KBr pellets but not in fused solid Cabosil pellets, suggesting the N_2O trapping is sensitive to the environment. N_2O yields were observed to be lower in the fused solids than in earlier measurements of thin films on ATR crystals but were similar to the yields measured from pure NN deposits on transmission windows.

In summary, the quantum yields and products from the commercial formulations in KBr are very similar to those for the pure NNs in KBr, suggesting that the use of the pure compounds in laboratory studies yields data relevant to actual use in the field. The one exception is photolysis of NPM at 350 nm, where increased water uptake by the additional ingredients in the formulation reduces the absorption cross section of NPM and hence its calculated quantum yield, whose true value may not in fact change in the absence of water uptake.

■ ASSOCIATED CONTENT

Supporting Information

The Supporting Information is available free of charge at https://pubs.acs.org/doi/10.1021/acsearthspacechem.1c00059.

SEM−EDS images of IMD embedded in KBr pellets; additional details on the infrared experimental methods; emission spectra of photolysis lamps; additional details on the HRMS experimental methods; infrared spectra of IMD degradation products, UR_{IMD} and DN_{IMD}; MS/MS analysis of species and proposed fragmentation pathways; HRMS data for DNF in solution showing *m/z*

https://doi.org/10.1021/acsearthspacechem.1c00059
ACS Earth Space Chem. 2021, 5, 1196−1209

203, 156, and 172; photolysis rate constants at 254 nm as a function of concentration; and details on quantum yield calculations using 2NB actinometer (PDF)

AUTHOR INFORMATION

Corresponding Author

Barbara J. Finlayson-Pitts − *Department of Chemistry, University of California Irvine, Irvine, California 92697-2025, United States;* orcid.org/0000-0003-4650-168X; Phone: (949) 824-7670; Email: bjfinlay@uci.edu; Fax: (949) 824-2420

Authors

Andrea Rohrbacher − *Department of Chemistry, University of California Irvine, Irvine, California 92697-2025, United States*

Michael J. Ezell − *Department of Chemistry, University of California Irvine, Irvine, California 92697-2025, United States*

Véronique Perraud − *Department of Chemistry, University of California Irvine, Irvine, California 92697-2025, United States;* orcid.org/0000-0003-1247-9787

Complete contact information is available at: https://pubs.acs.org/10.1021/acsearthspacechem.1c00059

Funding

This work was funded by the NSF (grant #1707883), the Ridge to Reef NSF Research Traineeship (award DGE-1735040), the Army Research Office DURIP equipment grant (#W911NF2010064), and the NSF Major Research Instrumentation Program (grant #1920242 and #1337080).

Notes

The authors declare no competing financial interest.

ACKNOWLEDGMENTS

The authors thank W. Wang and L. M. Wingen for assistance with the manuscript and helpful discussions. The authors also thank Sara Heedy who performed sputter coating and SEM at the Irvine Materials Research Institute (IMRI) at UC Irvine, as well as helpful discussions. We are also deeply grateful to Jorg Meyer for his skillful glass blowing work that made these experiments possible.

ABBREVIATIONS

NN, neonicotinoid; DNF, dinotefuran; NPM, nitenpyram; IMD, imidacloprid; CLD, clothianidin; ATR, attenuated total reflectance; FTIR, Fourier transform infrared spectroscopy; DART-MS, direct analysis in real time mass spectrometry; UPLC−DAD−HRMS, ultrahigh-pressure liquid chromatography coupled to a diode array detector and a high resolution orbitrap mass spectrometer

REFERENCES

(1) Simon-Delso, N.; Amaral-Rogers, V.; Belzunces, L. P.; Bonmatin, J. M.; Chagnon, M.; Downs, C.; Furlan, L.; Gibbons, D. W.; Giorio, C.; Girolami, V.; Goulson, D.; Kreutzweiser, D. P.; Krupke, C. H.; Liess, M.; Long, E.; McField, M.; Mineau, P.; Mitchell, E. A. D.; Morrissey, C. A.; Noome, D. A.; Pisa, L.; Settele, J.; Stark, J. D.; Tapparo, A.; Van Dyck, H.; Van Praagh, J.; Van der Sluijs, J. P.; Whitehorn, P. R.; Wiemers, M. Systemic insecticides (neonicotinoids and fipronil): trends, uses, mode of action and metabolites. *Environ. Sci. Pollut. Res.* **2015**, *22*, 5−34.

(2) Douglas, M. R.; Tooker, J. F. Large-scale deployment of seed treatments has driven rapid increase in use of neonicotinoid insecticides and preemptive pest management in US field crops. *Environ. Sci. Technol.* **2015**, *49*, 5088−5097.

(3) Jeschke, P.; Nauen, R.; Schindler, M.; Elbert, A. Overview of the status and global strategy for neonicotinoids. *J. Agric. Food Chem.* **2011**, *59*, 2897−2908.

(4) Jeschke, P.; Nauen, R. Neonicotinoids - from zero to hero in insecticide chemistry. *Pest Manage. Sci.* **2008**, *64*, 1084−1098.

(5) Elbert, A.; Haas, M.; Springer, B.; Thielert, W.; Nauen, R. Applied aspects of neonicotinoid uses in crop protection. *Pest Manage. Sci.* **2008**, *64*, 1099−1105.

(6) National Water-Quality Assessment (NAWQA) Program Annual Pesticides Use Maps. https://water.usgs.gov/nawqa/pnsp/usage/maps/ (accessed March 3, 2021).

(7) Tomizawa, M.; Casida, J. E. Neonicotinoid insecticide toxicology: Mechanisms of selective action. *Annu. Rev. Pharmacol. Toxicol.* **2005**, *45*, 247−268.

(8) Casida, J. E. Neonicotinoid metabolism: compounds, substituents, pathways, enzymes, organisms, and relevance. *J. Agric. Food Chem.* **2011**, *59*, 2923−2931.

(9) Debnath, B.; Gayen, S.; Basu, A.; Ghosh, B.; Srikanth, K.; Jha, T. Quantitative structure-activity relationship study using refractotopological state atom index on some neonicotinoid insecticides. *Bioorg. Med. Chem.* **2004**, *12*, 6137−6145.

(10) Zwart, R.; Oortgiesen, M.; Vijverberg, H. P. M. Nitromethylene heterocycles - selective agonists of nicotinic receptors in locust neurons compared to mouse N1e-115 and Bc3h1 cells. *Pestic. Biochem. Physiol.* **1994**, *48*, 202−213.

(11) Goulson, D. Review: An overview of the environmental risks posed by neonicotinoid insecticides. *J. Appl. Ecol.* **2013**, *50*, 977−987.

(12) Buchholz, A.; Nauen, R. Translocation and translaminar bioavailability of two neonicotinoid insecticides after foliar application to cabbage and cotton. *Pest Manage. Sci.* **2002**, *58*, 10−16.

(13) Halmer, P. Commercial seed treatment technology. In *Seed Technology and Its Biological Basis*; Black, M., Bewley, J.D., Eds.; CRC Press: U.K., Sheffield, 2000; pp 257−286.

(14) Sur, R.; Stork, A. Uptake, translocation and metabolism of imidacloprid in plants. *Bull. Insectol.* **2003**, *56*, 35−40.

(15) Wood, T. J.; Goulson, D. The environmental risks of neonicotinoid pesticides: a review of the evidence post 2013. *Environ. Sci. Pollut. Res.* **2017**, *24*, 17285−17325.

(16) Wintermantel, D.; Odoux, J.-F.; Decourtye, A.; Henry, M.; Allier, F.; Bretagnolle, V. Neonicotinoid-induced mortality risk for bees foraging on oilseed rape nectar persists despite EU moratorium. *Sci. Total Environ.* **2020**, *704*, 135400.

(17) George, C.; Ammann, M.; D'Anna, B.; Donaldson, D. J.; Nizkorodov, S. A. Heterogeneous photochemistry in the atmosphere. *Chem. Rev.* **2015**, *115*, 4218−4258.

(18) Lester, Y.; Sabach, S.; Zivan, O.; Dubowski, Y. Key environmental processes affecting the fate of the insecticide chloropyrifos applied to leaves. *Chemosphere* **2017**, *171*, 74−80.

(19) Kira, O.; Linker, R.; Dubowski, Y. Estimating drift of airborne pesticides during orchard spraying using active Open Path FTIR. *Atmos. Environ.* **2016**, *142*, 264−270.

(20) Estillore, A. D.; Trueblood, J. V.; Grassian, V. H. Atmospheric chemistry of bioaerosols: heterogeneous and multiphase reactions with atmospheric oxidants and other trace gases. *Chem. Sci.* **2016**, *7*, 6604−6616.

(21) Girolami, V.; Mazzon, L.; Squartini, A.; Mori, N.; Marzaro, M.; Di Bernardo, A.; Greatti, M.; Giorio, C.; Tapparo, A. Translocation of neonicotinoid insecticides from coated seeds to seedling guttation drops: a novel way of intoxication for bees. *J. Econ. Entomol.* **2009**, *102*, 1808−1815.

(22) Greatti, M.; Sabatini, A. G.; Barbatinni, R.; Rossi, S.; Stravasi, A. Risk of environmental contamination by the active ingredient imidacloprid used for corn seed dressing. *Bull. Insectol.* **2003**, *56*, 69−72.

(23) Craddock, H. A.; Huang, D.; Turner, P. C.; Quirós-Alcalá, L.; Payne-Sturges, D. C. Trends in neonicotinoid pesticide residues in food and water in the United States, 1999−2015. *Environ. Health* **2019**, *18*, 1−16.
(24) Lu, C.; Chang, C.-H.; Palmer, C.; Zhao, M.; Zhang, Q. Neonicotinoid residues in fruits and vegetables: an integrated dietary exposure assessment approach. *Environ. Sci. Technol.* **2018**, *52*, 3175−3184.
(25) Liu, S.; Zheng, Z.; Wei, F.; Ren, Y.; Gui, W.; Wu, H.; Zhu, G. Simultaneous determination of seven neonicotinoid pesticide residues in food by ultraperformance liquid chromatography tandem mass spectrometry. *J. Agric. Food Chem.* **2010**, *58*, 3271−3278.
(26) Mitchell, E. A. D.; Mulhauser, B.; Mulot, M.; Mutabazi, A.; Glauser, G.; Aebi, A. A worldwide survey of neonicotinoids in honey. *Science* **2017**, *358*, 109−111.
(27) Mullin, C. A.; Frazier, M.; Frazier, J. L.; Ashcraft, S.; Simonds, R.; vanEngelsdorp, D.; Pettis, J. S. High levels of miticides and agrochemicals in North American apiaries: implications for honey bee health. *PloS One* **2010**, *5*, 1−19.
(28) Goulson, D.; Nicholls, E.; Botias, C.; Rotheray, E. L. Bee declines driven by combined stress from parasites, pesticides, and lack of flowers. *Science* **2015**, *347*, 1255957.
(29) Bonmatin, J.-M.; Giorio, C.; Girolami, V.; Goulson, D.; Kreutzweiser, D. P.; Krupke, C.; Liess, M.; Long, E.; Marzaro, M.; Mitchell, E. A. D.; Noome, D. A.; Simon-Delso, N.; Tapparo, A. Environmental fate and exposure; neonicotinoids and fipronil. *Environ. Sci. Pollut. Res.* **2015**, *22*, 35−67.
(30) Botías, C.; David, A.; Horwood, J.; Abdul-Sada, A.; Nicholls, E.; Hill, E.; Goulson, D. Neonicotinoid residues in wildflowers, a potential route of chronic exposure for bees. *Environ. Sci. Technol.* **2015**, *49*, 12731−12740.
(31) Hladik, M. L.; Main, A. R.; Goulson, D. Environmental risks and challenges associated with neonicotinoid insecticides. *Environ. Sci. Technol.* **2018**, *52*, 3329−3335.
(32) Stehle, S.; Schulz, R. Agricultural insecticides threaten surface waters at the global scale. *Proc. Natl. Acad. Sci. U.S.A.* **2015**, *112*, 5750−5755.
(33) Morrissey, C. A.; Mineau, P.; Devries, J. H.; Sanchez-Bayo, F.; Liess, M.; Cavallaro, M. C.; Liber, K. Neonicotinoid contamination of global surface waters and associated risk to aquatic invertebrates: A review. *Environ. Int.* **2015**, *74*, 291−303.
(34) Fischer, J.; Muller, T.; Spatz, A. K.; Greggers, U.; Grunewald, B.; Menzel, R. Neonicotinoids interfere with specific components of navigation in honeybees. *PloS One* **2014**, *9*, No. e91364.
(35) Pisa, L. W.; Amaral-Rogers, V.; Belzunces, L. P.; Bonmatin, J. M.; Downs, C. A.; Goulson, D.; Kreutzweiser, D. P.; Krupke, C.; Liess, M.; McField, M.; Morrissey, C. A.; Noome, D. A.; Settele, J.; Simon-Delso, N.; Stark, J. D.; Van der Sluijs, J. P.; Van Dyck, H.; Wiemers, M. Effects of neonicotinoids and fipronil on non-target invertebrates. *Environ. Sci. Pollut. Res.* **2015**, *22*, 68−102.
(36) Crall, J. D.; Switzer, C. M.; Oppenheimer, R. L.; Ford Versypt, A. N.; Dey, B.; Brown, A.; Eyster, M.; Guérin, C.; Pierce, N. E.; Combes, S. A.; de Bivort, B. L. Neonicotinoid exposure disrupts bumblebee nest behavior, social networks, and thermoregulation. *Science* **2018**, *362*, 683−686.
(37) Rundlöf, M.; Andersson, G. K. S.; Bommarco, R.; Fries, I.; Hederström, V.; Herbertsson, L.; Jonsson, O.; Klatt, B. K.; Pedersen, T. R.; Yourstone, J.; Smith, H. G. Seed coating with a neonicotinoid insecticide negatively affects wild bees. *Nature* **2015**, *521*, 77−80.
(38) Tsvetkov, N.; Samson-Robert, O.; Sood, K.; Patel, H. S.; Malena, D. A.; Gajiwala, P. H.; Maciukiewicz, P.; Fournier, V.; Zayed, A. Chronic exposure to neonicotinoids reduces honey bee health near corn crops. *Science* **2017**, *356*, 1395−1397.
(39) Blacquière, T.; Smagghe, G.; Van Gestel, C. A. M.; Mommaerts, V. Erratum to: Neonicotinoids in bees: a review on concentrations, side-effects and risk assessment. *Ecotoxicology* **2012**, *21*, 1581.
(40) Whitehorn, P. R.; O'Connor, S.; Wackers, F. L.; Goulson, D. Neonicotinoid pesticide reduces bumble bee colony growth and queen production. *Science* **2012**, *336*, 351−352.
(41) Kadlikova, K.; Vaclavikova, M.; Halesova, T.; Kamler, M.; Markovic, M.; Erban, T. The investigation of honey bee pesticide poisoning incidents in Czechia. *Chemosphere* **2021**, *263*, 128056.
(42) Woodcock, B. A.; Bullock, J. M.; Shore, R. F.; Heard, M. S.; Pereira, M. G.; Redhead, J.; Ridding, L.; Dean, H.; Sleep, D.; Henrys, P.; Peyton, J.; Hulmes, S.; Hulmes, L.; Sárospataki, M.; Saure, C.; Edwards, M.; Genersch, E.; Knäbe, S.; Pywell, R. F. Country-specific effects of neonicotinoid pesticides on honey bees and wild bees. *Science* **2017**, *356*, 1393−1395.
(43) Chao, S. L.; Casida, J. E. Interaction of imidacloprid metabolites and analogs with the nicotinic acetylcholine receptor of mouse brain in relation to toxicity. *Pestic. Biochem. Physiol.* **1997**, *58*, 77−88.
(44) European Commission. *Commission Implementing Regulation (EU) 2018/783 of 29 May 2018, Implementing Regulation (EU) No 540/2011 as Regards the Conditions of Approval of the Active Substance Imidacloprid, Clothianidin, and Thiamethoxam*; Official Journal of the European Union: Brussels, 2018; Vol. *L*, pp 31−44.
(45) Stokstad, E. European agency concludes controversial 'neonic' pesticides threaten bees. *Science* **2018**, *2018*, 1321.
(46) Wang, W.; Aregahegn, K. Z.; Andersen, S. T.; Ni, A. Z.; Rohrbacher, A. F.; Nielsen, O. J.; Finlayson-Pitts, B. J. Quantum Yields and N_2O Formation from Photolysis of Solid Films of Neonicotinoids. *J. Agric. Food Chem.* **2019**, *67*, 1638−1646.
(47) Aregahegn, K. Z.; Shemesh, D.; Gerber, R. B.; Finlayson-Pitts, B. J. Photochemistry of thin solid films of the neonicotinoid imidacloprid on surfaces. *Environ. Sci. Technol.* **2017**, *51*, 2660−2668.
(48) Aregahegn, K. Z.; Ezell, M. J.; Finlayson-Pitts, B. J. Photochemistry of solid films of the neonicotinoid nitenpyram. *Environ. Sci. Technol.* **2018**, *52*, 2760−2767.
(49) *CRC Handbook of Chemistry and Physics*; Rumble, J. R., Ed.; CRC Press/Taylor & Francis: Boca Raton, Fl, 2020.
(50) Valent. *Safari 20SG Insecticide Safety Data Sheet*. SDS No 0426, 2015.
(51) FDA Professional Drug Information Database. https://www.drugs.com/pro/capstar.html (accessed March 3, 2021).
(52) Le Questel, J.-Y.; Graton, J.; Cerón-Carrasco, J. P.; Jacquemin, D.; Planchat, A.; Thany, S. H. New insights on the molecular features and electrophysiological properties of dinotefuran, imidacloprid and acetamiprid neonicotinoid insecticides. *Bioorg. Med. Chem.* **2011**, *19*, 7623−7634 Figure 9 is adapted from this paper with permission of Elsevier.
(53) Noestheden, M.; Roberts, S.; Hao, C. Nitenpyram degradation in finished drinking water. *Rapid Commun. Mass Spectrom.* **2016**, *30*, 1653−1661.
(54) Socrates, G. *Infrared and Raman Characteristic Group Frequencies: Tables and Charts*, 3rd ed.; John Wiley & Sons Ltd.: West Sussex, England, 2001.
(55) Raina-Fulton, R.; Behdarvandan, A. Liquid chromatography-mass spectrometry for the determination of neonicotinoid insecticides and their metabolites in biological, environmental and food commodity matrices. *Trends Chromatogr.* **2016**, *10*, 51−79.
(56) Kamel, A. Refined Methodology for the Determination of Neonicotinoid Pesticides and Their Metabolites in Honey Bees and Bee Products by Liquid Chromatography−Tandem Mass Spectrometry (LC-MS/MS)†. *J. Agric. Food Chem.* **2010**, *58*, 5926−5931.
(57) Yang, Z.; Zhang, K.; Chen, L.; Liu, B.; Zhang, Q.; Zhang, H.; Sun, C.; Hu, D. Determination of dinotefuran and its metabolites in orange pulp, orange peel, and whole orange using liquid chromatography-tandem mass spectrometry. *J. AOAC Int.* **2017**, *100*, 1551−1558.
(58) Kamel, A.; Qian, Y.; Kolbe, E.; Stafford, C. Development and validation of a multiresidue method for the determination of neonicotinoid and macrocyclic lactone pesticide residues in milk, fruits, and vegetables by ultra-performance liquid chromatography/MS/MS. *J. AOAC Int.* **2010**, *93*, 389−399.

(59) Xie, W.; Han, C.; Qian, Y.; Ding, H.; Chen, X.; Xi, J. Determination of neonicotinoid pesticides residues in agricultural samples by solid-phase extraction combined with liquid chromatography-tandem mass spectrometry. *J. Chromatogr. A* **2011**, *1218*, 4426−4433.
(60) EPA. U. S Dinotefuran Pesticide Fact Sheet. https://www3.epa.gov/pesticides/chem_search/reg_actions/registration/fs_PC-044312_01-Sep-04.pdf (accessed March 3, 2021).
(61) Laane, J.; Ohlsen, J. R. Characterization of nitrogen oxides by vibrational spectroscopy. *Prog. Inorg. Chem.* **1980**, *27*, 465−513.
(62) Coblentz Society Inc. Evaluated Infrared Reference Spectra. In *NIST Chemistry WebBook, NIST Standard Reference Database Number 69*; Linstrom, P. J., Mallard, W. G., Eds., 2018.
(63) Dows, D. A. Infrared spectrum of solid nitrous oxide. *J. Chem. Phys.* **1957**, *26*, 745−747.
(64) Yamada, H.; Person, W. B. Absolute Infrared Intensities of the Fundamental Absorption Bands in Solid CO_2 and N_2O. *J. Chem. Phys.* **1964**, *41*, 2478−2487.
(65) Hisatsune, I. C. Infrared Spectrum of Matrix-Isolated Nitrous Oxide. *J. Chem. Phys.* **1972**, *57*, 2631−2636.
(66) Hadjiivanov, K.; Saussey, J.; Freysz, J. L.; Lavalley, J. C. FT-IR study of NO + O_2 co-adsorption on H-ZSM-5: re-assignment of the 2133 cm^{-1} band to NO^+ species. *Catal. Lett.* **1998**, *52*, 103−108.
(67) Pommier, B.; Gelin, P. Infrared and volumetric study of NO adsorption on Pd-H-ZSM-5. *Phys. Chem. Chem. Phys.* **2001**, *3*, 1138−1143.
(68) Hadjiivanov, K.; Knözinger, H. Species formed after NO adsorption and NO + O_2 co-adsorption on TiO_2: an FTIR spectroscopic study. *Phys. Chem. Chem. Phys.* **2000**, *2*, 2803−2806.
(69) Lobree, L. J.; Hwang, I. C.; Reimer, J. A.; Bell, A. T. An in situ infrared study of NO reduction by C_3H_8 over Fe-ZSM-5. *Catal. Lett.* **1999**, *63*, 233−240.
(70) Konduru, M. V.; Chuang, S. S. C. Dynamics of NO and N_2O Decomposition over Cu-ZSM-5 under Transient Reducing and Oxidizing Conditions. *J. Catal.* **2000**, *196*, 271−286.
(71) Joyner, R.; Stockenhuber, M. Preparation, Characterization, and Performance of Fe−ZSM-5 Catalysts. *J. Phys. Chem. B* **1999**, *103*, 5963−5976.
(72) Hadjiivanov, K. I. IR study of CO and NOx sorption on Ag-ZSM-5. *Microporous Mesoporous Mater.* **1998**, *24*, 41−49.
(73) Gerlach, T.; Schütze, F.-W.; Baerns, M. An FTIR Study on the Mechanism of the Reaction between Nitrogen Dioxide and Propene over Acidic Mordenites. *J. Catal.* **1999**, *185*, 131−137.
(74) Chen, H.-Y.; Voskoboinikov, T.; Sachtler, W. M. H. Reduction of NOx over Fe/ZSM-5 catalysts: mechanistic causes of activity differences between alkanes. *Catal. Today* **1999**, *54*, 483−494.
(75) Gélin, P.; Goguet, A.; Descorme, C.; Lécuyer, C.; Primet, M. Catalytic properties of palladium exchanged ZSM-5 catalysts in the reduction of nitrogen monoxide by methane in the presence of oxygen: Nature of the active sites. *Stud. Surf. Sci. Catal.* **1998**, *116*, 275−284.
(76) Finlayson-Pitts, B. J.; Johnson, S. N. The reaction of NO_2 with NaBr: Possible source of BrNO in polluted marine atmospheres. *Atmos. Environ.* **1988**, *22*, 1107−1112.
(77) Calvert, J. G.; Pitts, J. N. *Photochemistry*; John Wiley & Sons, Inc., 1966.
(78) Klan, P.; Wirz, J. *Photochemistry of Organic Compounds: From Concepts to Practice*; John Wiley & Sons, Ltd., 2009.
(79) Bhattacharya, A.; Guo, Y. Q.; Bernstein, E. R. Experimental and theoretical exploration of the initial steps in the decomposition of a model nitramine energetic material: dimethylnitramine. *J. Phys. Chem. A* **2009**, *113*, 811−823.
(80) Groffman, P. M.; Butterbach-Bahl, K.; Fulweiler, R. W.; Gold, A. J.; Morse, J. L.; Stander, E. K.; Tague, C.; Tonitto, C.; Vidon, P. Challenges to incorporating spatially and temporally explicit phenomena (hotspots and hot moments) in denitrification models. *Biogeochemistry* **2009**, *93*, 49−77.
(81) Groffman, P. M.; Altabet, M. A.; Böhlke, J. K.; Butterbach-Bahl, K.; David, M. B.; Firestone, M. K.; Giblin, A. E.; Kana, T. M.; Nielsen, L. P.; Voytek, M. A. Methods for measuring denitrification: diverse approaches to a difficult problem. *Ecol. Appl.* **2006**, *16*, 2091−2122.
(82) Wolf, B.; Zheng, X.; Brüggemann, N.; Chen, W.; Dannenmann, M.; Han, X.; Sutton, M. A.; Wu, H.; Yao, Z.; Butterbach-Bahl, K. Grazing-induced reduction of natural nitrous oxide release from continental steppe. *Nature* **2010**, *464*, 881−884.
(83) Fowler, D.; Pilegaard, K.; Sutton, M. A.; Ambus, P.; Raivonen, M.; Duyzer, J.; Simpson, D.; Fagerli, H.; Fuzzi, S.; Schjoerring, J. K.; Granier, C.; Neftel, A.; Isaksen, I. S. A.; Laj, P.; Maione, M.; Monks, P. S.; Burkhardt, J.; Daemmgen, U.; Neirynck, J.; Personne, E.; Wichink-Kruit, R.; Butterbach-Bahl, K.; Flechard, C.; Tuovinen, J. P.; Coyle, M.; Gerosa, G.; Loubet, B.; Altimir, N.; Gruenhage, L.; Ammann, C.; Cieslik, S.; Paoletti, E.; Mikkelsen, T. N.; Ro-Poulsen, H.; Cellier, P.; Cape, J. N.; Horváth, L.; Loreto, F.; Niinemets, Ü.; Palmer, P. I.; Rinne, J.; Misztal, P.; Nemitz, E.; Nilsson, D.; Pryor, S.; Gallagher, M. W.; Vesala, T.; Skiba, U.; Brüggemann, N.; Zechmeister-Boltenstern, S.; Williams, J.; O'Dowd, C.; Facchini, M. C.; de Leeuw, G.; Flossman, A.; Chaumerliac, N.; Erisman, J. W. Atmospheric composition change: Ecosystems-Atmosphere interactions. *Atmos. Environ.* **2009**, *43*, 5193−5267.
(84) Finlayson-Pitts, B. J.; Pitts, J. N. *Chemistry of the Upper and Lower Atmosphere: Theory, Experiments, and Application*; Academic Press: San Diego, 2000.
(85) Leighton, P. A.; Lucy, F. A. The Photoisomerization of the o-Nitrobenzaldehydes I. Photochemical Results. *J. Chem. Phys.* **1934**, *2*, 756−759.
(86) Pitts, J. N.; Wan, J. K. S.; Schuck, E. A. Photochemical studies in an alkali halide matrix. I. An o-nitrobenzaldehyde actinometer and its application to a kinetic study of the photoreduction of benzophenone by benzhydrol in a pressed potassium bromide disk. *J. Am. Chem. Soc.* **1964**, *86*, 3606−3610.
(87) Vichutinskaya, E. V.; Postnikov, L. M.; Kushnerev, M. Y. Use of ortho-nitrobenzaldehyde as an internal actinometer in investigation of photooxidative degradation of thin unoriented polycaproamide films. *Vysokomol. Soedin., Ser. A* **1975**, *17*, 621−625.
(88) Allen, J. M.; Allen, S. K.; Baertschi, S. W. 2-Nitrobenzaldehyde: a convenient UV-A and UV-B chemical actinometer for drug photostability testing. *J. Pharm. Biomed. Anal.* **2000**, *24*, 167−178.
(89) Liu, R. S. H.; Hammond, G. S. Reflection on medium effects on photochemical reactivity. *Acc. Chem. Res.* **2005**, *38*, 396−403.
(90) Ezell, M. J.; Wang, W.; Shemesh, D.; Ni, A.; Gerber, R. B.; Finlayson-Pitts, B. J. Experimental and theoretical studies of the environmental sensitivity of the absorption spectra and photochemistry of nitenpyram and analogs. *ACS Earth Space Chem.* **2019**, *3*, 2063−2075.

https://doi.org/10.1021/acsearthspacechem.1c00059
ACS Earth Space Chem. 2021, 5, 1196−1209